



Performance assessment of the ALBIRA II pre-clinical SPECT S102 system for ^{99m}Tc imaging

Ali Asgar Attarwala¹ · Deni Hardiansyah^{1,2} · Chiara Romanó¹ · Luis David Jiménez-Franco^{1,3} · Mareike Roscher^{4,5} · Björn Wängler⁴ · Gerhard Glatting^{1,6}

Received: 22 April 2020 / Accepted: 29 October 2020 / Published online: 12 November 2020
© The Japanese Society of Nuclear Medicine 2020

Abstract

Objective The performance characteristics of the SPECT sub-system S102 of the ALBIRA II PET/SPECT/CT are analyzed for the 80 mm field of view (FOV) to evaluate the potential *in-vivo* imaging in rats, based on measurements of the system response for the commonly used Technetium-99 m (^{99m}Tc) in small animal imaging.

Methods The ALBIRA II tri-modal $\mu\text{PET/SPECT/CT}$ pre-clinical system (Bruker BioSpin, Ettlingen, Germany) was used. The SPECT modality is made up of two opposite gamma cameras (Version S102) with Sodium doped Cesium Iodide (CsI(Na)) single continuous crystal detectors coupled to position-sensitive photomultipliers (PSPMTs). Imaging was performed with the NEMA NU-4 image quality phantom (Data Spectrum Corporation, Durham, USA). Measurements were performed with a starting activity concentration of 4.76 MBq/mL ^{99m}Tc . An energy window of 20% at 140 keV was selected in this study. The system offers a 20 mm, 40 mm, 60 mm and an 80 mm field of view (FOV) and in this study the 80 mm FOV was used for all the acquisitions. The data were reconstructed with an ordered subset expectation maximization (OSEM) algorithm. Sensitivity, spatial resolution, count rate linearity, convergence of the algorithm and the recovery coefficients (RC) were analyzed. All analyses were performed with PMOD and MATLAB software.

Results The sensitivities measured at the center of the 80 mm FOV with the point source were 23.1 ± 0.3 cps/MBq (single pinhole SPH) and 105.6 ± 5.5 cps/MBq (multi pinhole MPH). The values for the axial, tangential and radial full width at half maximum (FWHM) were 2.51, 2.54, and 2.55 mm with SPH and 2.35, 2.44 and 2.32 mm with MPH, respectively. The corresponding RC values for the 5 mm, 4 mm, 3 mm and 2 mm rods were 0.60 ± 0.28 , 0.61 ± 0.24 , 0.29 ± 0.11 and 0.20 ± 0.06 with SPH and 0.56 ± 0.20 , 0.50 ± 0.18 , 0.38 ± 0.09 and 0.23 ± 0.06 with MPH. To obtain quantitative imaging data, the image reconstructions should be performed with 12 iterations.

Conclusion The ALBIRA II preclinical SPECT sub-system S102 has a favorable sensitivity and spatial resolution for the 80 mm FOV setting for both the SPH and MPH configurations and is a valuable tool for small animal imaging.

Keywords SPECT · ALBIRA · Pre-clinical imaging

Ali Asgar Attarwala and Deni Hardiansyah contributed equally to this work.

✉ Deni Hardiansyah
denihardiansyah@ui.ac.id

¹ Medical Radiation Physics/Radiation Protection, Universitätsmedizin Mannheim, Medical Faculty Mannheim, Heidelberg University, 68167 Mannheim, Germany

² Medical Physics and Biophysics Research Group, Physics Department, Faculty of Mathematics and Natural Sciences (FMIPA), Universitas Indonesia, Depok 16424, Indonesia

³ ABX-CRO Advanced Pharmaceutical Services Forschungsgesellschaft GmbH, 01307 Dresden, Germany

⁴ Molecular Imaging and Radiochemistry, Department for Clinical Radiology and Nuclear Medicine, Medical Faculty Mannheim, Heidelberg University, 68167 Mannheim, Germany

⁵ Radiooncology/Radiobiology, German Cancer Research Center (DKFZ), 69120 Heidelberg, Germany

⁶ Medical Radiation Physics, Department of Nuclear Medicine, Ulm University, 89081 Ulm, Germany

Introduction

Quantitative imaging with a pre-clinical single-photon emission computed tomography (SPECT) is frequently used in research with small animal models such as mice and rats as part of the process for the development of diagnostic and therapeutic radiopharmaceuticals. These *in-vivo* preclinical studies allow for evaluating the effectiveness of new radioactive drugs prior to translation to clinical applications [1–3]. In addition, the combination of such a molecular imaging device with computed tomography (CT) provides both structural and functional data allowing a better analysis of the study images [4, 5].

Analysis of the performance of a molecular imaging system based on its physical characteristics is an important task to obtain reliable quantitative images. Factors such as the system sensitivity, detector linearity, spatial resolution, recovery coefficients and adequate reconstruction parameters are essential for quantitative imaging [6]. Quantitative images are important in molecular radiotherapy for obtaining accurate biokinetic parameters and dose calculations [7–9]. Knowing the characteristics of an imaging system may allow improvements in the images (precision) and in their quantitation. Thus, for example, based on the intrinsic point-spread function (PSF) of an imaging system for a specific radionuclide, some filters or other image processing techniques can be used to improve the image spatial resolution. In addition, the system sensitivity can be used to optimize the amount of injected activity to ensure adequate image quality. Eventually, the characterization of the system may allow improvements in the reconstruction algorithm or the application of advanced post-processing techniques.

The ALBIRA II pre-clinical SPECT sub-system S102 is part of the second generation trimodal ALBIRA II PET/SPECT/CT system (Bruker BioSpin, Ettlingen, Germany), which additionally includes imaging capabilities for positron emission tomography (PET) and computed tomography (CT). The ALBIRA II SPECT system with the S102 model gamma camera has the same configuration as the ALBIRA I SPECT system. The improvements in the ALBIRA II system as compared to its predecessor were related to PET electronics and hardware. Note that today, Bruker has introduced a new, third generation ALBIRA system (ALBIRA Si), that includes silicon-PM (Si) based PET technology and a new SPECT camera design (called S108) that forms the ALBIRA Si imaging platform, and that is different from the ALBIRA II system generation evaluated in this study.

In our previous study [10], the imaging characteristics of the Albira II PET sub-system and the response of the system for the radionuclides Fluorine-18 (^{18}F), Gallium-68

(^{68}Ga) and Copper-64 (^{64}Cu) were analyzed. The ALBIRA II SPECT sub-system offers flexibility to the end user with several fields of views (FOVs) and collimator configurations. In this study, the performance characteristics of the device are analyzed for the 80 mm FOV with the single pinhole (SPH) and multi-pinhole (MPH) collimators to evaluate the potential of *in-vivo* imaging in rats, based on measurements of the system response for the commonly used radionuclide Technetium-99 m ($^{99\text{m}}\text{Tc}$) in small animal imaging.

Materials and methods

SPECT imaging system

The SPECT sub-system of the ALBIRA II tri-modal system consists of two opposite gamma cameras (S102 model) with Sodium doped Cesium Iodide (CsI(Na)) single continuous crystal detectors with an area of $50 \times 50 \text{ mm}^2$ and a thickness of 4 mm, coupled to position-sensitive photomultipliers (PSPMTs). Each camera can rotate 180 degrees with a step size of 6 degrees, enabling a total of 60 projections. The SPECT system can operate with the SPH and/or the MPH collimation system. In the SPH case a knife-edge type hole of 2-mm thickness is drilled in a tungsten foil. The inner diameter of 1 mm and the outer diameter of 2 mm allow an acceptance angle of 53 degrees and a focal length of $f=31 \text{ mm}$. The MPH has a focal length of $f=31 \text{ mm}$ and has five holes drilled in a 2 mm thick tungsten foil. The diagonal apertures are located 4 mm from the central hole [11]. Four different fields of view (FOVs) are available with diameters of 20 mm, 40 mm, 60 mm and 80 mm, respectively [11]. However, this study shows analyses only with the 80 mm FOV. In this study, we investigated 80 mm FOV because (1) the 80 mm FOV is relevant for rat *in-vivo* imaging and has been used in preclinical studies [12] and (2) the phantom used in this study allowed only this FOV to be investigated. The ALBIRA II software suite (version 09-00128, Bruker Corporation, Ettlingen, Germany, 2012) was used for all data acquisitions and reconstructions.

Phantom measurements

To simulate the activity distribution and uptake in a small animal, a phantom designed by the National Electricals Manufacturers Association (NEMA) organization was employed during the experiments. The NEMA NU-4 image quality phantom (NEMA IQ) (Data Spectrum Corporation, Durham, USA) is 63 mm long, 33.5 mm in diameter, and has a side wall thickness of 1.5 mm. The phantom is divided into three main regions. The first one is a uniform fillable cylindrical section with a diameter of

30 mm used to generate a background region. The second part consists of 5 fillable rods with diameters of 1 mm, 2 mm, 3 mm, 4 mm and 5 mm. The rods are 20 mm long and are used to generate hot regions. The third region is a lid that is attached to the uniform region, enclosing two smaller hollow cylindrical chambers of 14 mm in length with an outer diameter of 8 mm and a wall thickness of 1 mm. For the measurements, one of the chambers is filled with non-radioactive water and the other with non-radioactive air.

In this study, measurements were performed with ^{99m}Tc with radioactivity amounts as described in “SPECT performance analysis” section. To estimate the background counts, acquisitions with the same settings and setup were additionally performed with the phantom filled with non-radioactive water placed in the FOV.

The data were reconstructed with an ordered subset expectation maximization (OSEM) algorithm and isotropic voxel sizes of 0.85 mm (SPH) and 1.0 mm (MPH) using an optimized number of iterations (between 2 to 30, see “Region of interest (ROI) analysis” section) and 12 subsets. The reconstructed images were used to analyze the system sensitivity and its recovery coefficients. Analyses were performed with the PMOD software version 3.6 (PMOD Technologies Ltd., Zurich, Switzerland).

Furthermore, an in-house phantom (Fig. 1a) was developed of polymethylmethacrylate (PMMA) with dimensions of $(60 \times 60 \times 10) \text{ mm}^3$ containing cylindrical capillaries (Fig. 1b) with a diameter of 1 mm [10]. This phantom was used to measure the spatial resolution of the system at the centre of the FOV.

SPECT performance analysis

Linearity and sensitivity assessments

To measure the sensitivity of the system, both the NEMA IQ and the point source phantom were used. The NEMA IQ phantom was uniformly filled with radioactivity. To measure sensitivity with the point-source phantom, a capillary was filled with a $1 \mu\text{L}$ ^{99m}Tc point-source solution positioned at the geometric centre of the FOV. The mean activity was 0.39 MBq for the SPH and 0.13 MBq for the MPH. Both the NEMA IQ and the point-source phantoms were scanned with the SPH and MPH collimators. The sensitivity of the detectors was calculated as the ratio between the total number of events per second (corrected for background) and the calibrated activity in the phantom.

The linearity of the system was evaluated by measuring the NEMA IQ phantom initially filled with an activity concentration of $\sim 4760 \text{ kBq/mL}$ until the time in which the activity concentration decayed to a negligible amount (twelve time-points, each measured for 60 min). The resulting counts per second (cps) y were plotted against the decay corrected activity x and fitted to a paralyzable system function [13]:

$$y = a \cdot (x + B) \cdot \exp(-(x + B) \cdot t) \quad (1)$$

where a is the sensitivity of the system [cps MBq^{-1}], B is the background activity [MBq] and t is the dead-time [MBq^{-1}].

The linearity of radioactivity and SPECT image count was investigated to assess the quantitative abilities of the system. The data acquired to analyse the sensitivity of the system with the NEMA image quality phantom were used. All the measurements were reconstructed using 12 iterations

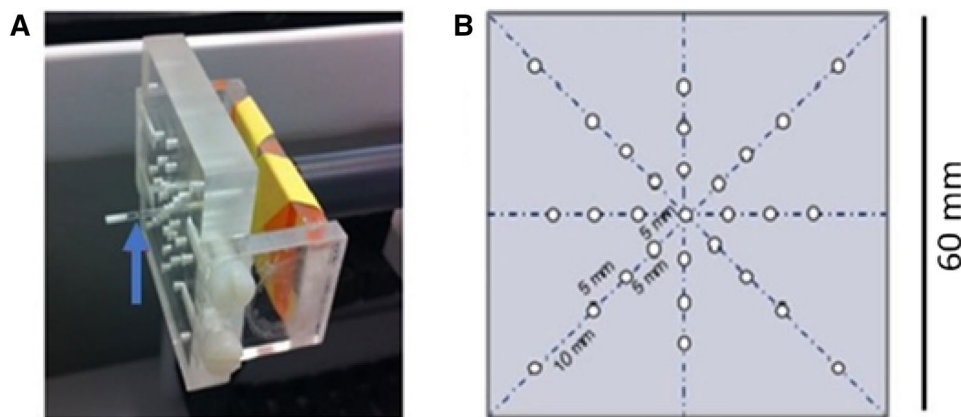


Fig. 1 **a** In-house developed phantom using polymethylmethacrylate (PMMA) for spatial resolution measurement using capillaries (blue arrow indicates the location of the drop of respective radionuclide activity). **b** The dimension of the phantom was $(60 \times 60 \times 10) \text{ mm}^3$

and contained cylindrical capillaries with a diameter of 1 mm, the holes were located on the transaxial and diagonal axes, with each of them 5 mm apart. The four most distant points on the diagonal direction were located 25 mm from the centre [10]

(algorithm converged at this iteration number, “[Region of interest \(ROI\) analysis](#)” section). The measurement was done according to NEMA protocol, a VOI was drawn in the centre of the uniform region of the NEMA image quality phantom with a 22.5 mm diameter and a 10.2 mm height for the SPH (12 slices) and 10 mm height for the MPH (10 slices). The data were also fitted to the paralyzable function shown in Eq. (1).

Region of interest (ROI) analysis

Measurements were performed with the NEMA IQ phantom filled with ^{99m}Tc and an activity concentration of ~ 394 kBq/mL and acquisition time of 30 min. The recovery coefficients (RC) were calculated as the ratio of the apparent activity in the rods and the activity in the uniform region.

The optimal number of iterations needed to obtain quantitative image data with ^{99m}Tc was identified by defining a convergence criterion for the reconstruction algorithm. The definition of the convergence criterion was based on the calculation of the variability (Var) according to [14]:

$$\text{Var} = (\text{STD}^2 + \Delta p^2)^{0.5}, \quad (2)$$

where *STD* is the standard deviation of the measured parameter (activity concentration in kBq/mL) and Δp is the difference between the measured parameter and the reference value. The reconstruction algorithm was considered to be converged when the Var of the measured parameter from the reference was minimal.

Spatial resolution

Measurements were performed using the in-house point-source phantom described in “[Phantom measurements](#)” section, filled with a 1 μL point source solution of ^{99m}Tc positioned at the geometric centre of the FOV. The mean activities were 0.75 MBq and 0.69 MBq for SPH and MPH collimation system, respectively. Since an internationally accepted standard for the performance assessment of a SPECT system does not exist, we followed the methodologies described in the NEMA NU-4 2008 standards (i.e. the accepted criteria to characterize PET systems) for the spatial resolution calculations at the center of the detector’s FOV for the *x*, *y* and *z* directions [15, 16]. The images were reconstructed using the OSEM algorithm. The central slice with the maximum pixel intensity was selected followed by summing up all the one-dimensional line profiles parallel to the investigated orientation (*x*, *y* or *z*). Parameters of a parabolic function were fitted to the maximum pixel and its two neighboring pixels to find the absolute maximum pixel intensity of the interpolated curve. Finally, the full width at half maximum (FWHM) is determined using half

of this maximum value and the full width at tenth maximum (FWTM) is determined using tenth of the maximum value by interpolation.

Additionally, this FWHM was corrected for the dimensions of the image pixel and the point-source. The blurring caused by the system response can be approximated by a Gaussian function [10]. The one-dimensional profile of the cylindrical source was approximated to a rectangular function in *x*, *y* and *z* directions. As a first approximation, these rectangular functions can be represented also by Gaussian functions with the same area under the curve and the same height as the rectangular functions. Hence, the corrected FWHM of the device is obtained according to:

$$(\text{FWHM}_d)^2 = (\text{FWHM}_m)^2 - (\text{FWHM}_s)^2, \quad (3)$$

where FWHM_d , FWHM_m and FWHM_s correspond to the FWHM of the detector, the measured (convoluted) FWHM and the source FWHM, respectively. We use this approximation for a Gaussian distribution to correct for the dimensions of the source. All the analyses were performed using MATLAB (R2015a, MathWorks, Natick, Massachusetts, USA).

Image uniformity

The evaluation of the image uniformity was performed following the NEMA protocol [16]. A cylindrical VOI was drawn in the center of the uniform region of the NEMA IQ phantom. The PMOD program was used to perform the analysis. The following parameters were recorded: the average activity concentration; the integral uniformity; the percentage standard deviation; the minimum and maximum values in the VOI [16].

The integral uniformity (3) was defined as follows:

Integral uniformity

$$= \frac{\text{maximum voxel value} - \text{minimum voxel value}}{\text{maximum voxel value} + \text{minimum voxel value}}, \quad (4)$$

The coefficient of variation (CV) was defined as follows:

$$\text{CV} = \frac{\text{voxel_STD}}{\text{mean_voxel_value}}, \quad (5)$$

where *voxel_STD* and *mean_voxel_value* are the standard deviation and the mean value of the voxel activity in the VOI. To investigate the image uniformity, the integral uniformity was plotted as a function of the injected activity (iteration number was fixed to 12) and as a function of the number of iterations (the activities were 8.10 MBq and 25.03 MBq).

Results

Linearity and sensitivity assessments

Figure 2 shows NEMA NU-4 phantom images for (A) the cylindrical rods, (B) the uniform region and (C) the two chambers filled with air and water. Images were acquired with the MPH collimator configuration and reconstructed with 2 iterations. The count rate linearity of the system

and SPECT image with both the SPH and MPH configuration plotted as a function of the activity are shown in Figs. 3 and 4, respectively. For both system and SPECT image linearity, the count rate per second (cps) showed a linear increase with activity for the SPH configuration. Using the MPH configuration, a deviation of around 17% was observed for activity of 100 MBq for SPECT image linearity. The effect of dead-time to the cps was analyzed by fitting a paralyzable function to the cps-activity curves (Figs. 3b and 4b). As a result, the fitting showed good fits

Fig. 2 The NEMA NU-4 phantom image showing (a and d) the cylindrical rods, (b and e) uniform region and (c and f) the two chambers filled with air and water. Images were acquired with the SPH (a, b and c) and MPH (d, e and f) collimator configurations using an activity of ~25 MBq, and were reconstructed with 2 iterations. Line profiles are shown for both SPH and MPH configurations in the cylindrical rods (g), uniform region (h) and two chambers (i). The horizontal line profiles were drawn through the center of 5 mm rods (a and d) and through the center of the images (b, c, e and f)

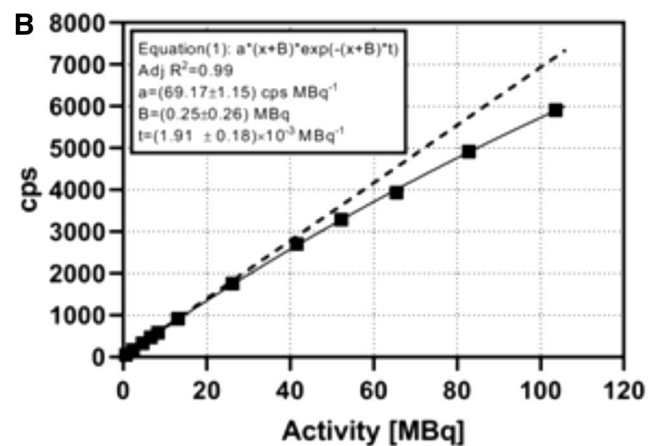
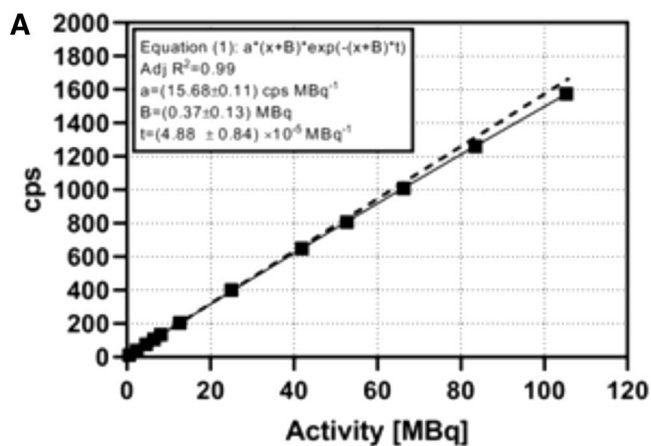
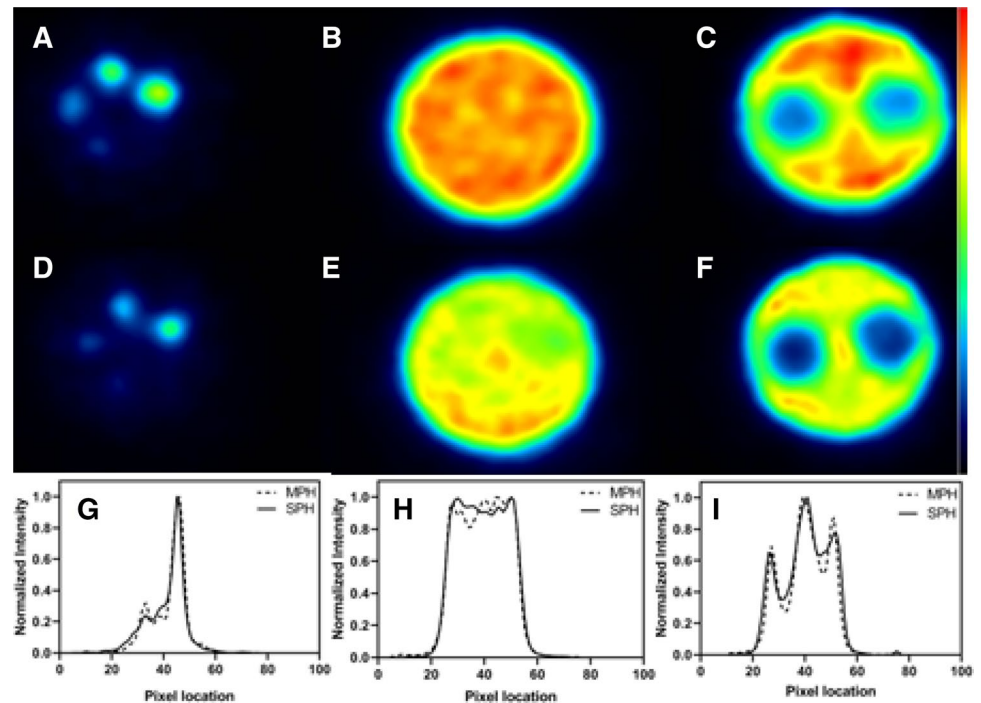


Fig. 3 System linearity for the SPH (a) and MPH (b) configuration with the fit parameters obtained from the paralyzable system function Eq. (1). The straight line corresponds to the case with $t=0$ MBq⁻¹. MPH configuration shows slight bending for higher activities because

of five times higher counts as compared to the SPH configuration, however, (Eq. 1) was successfully used to describe this bending and can be used for correcting the deviation

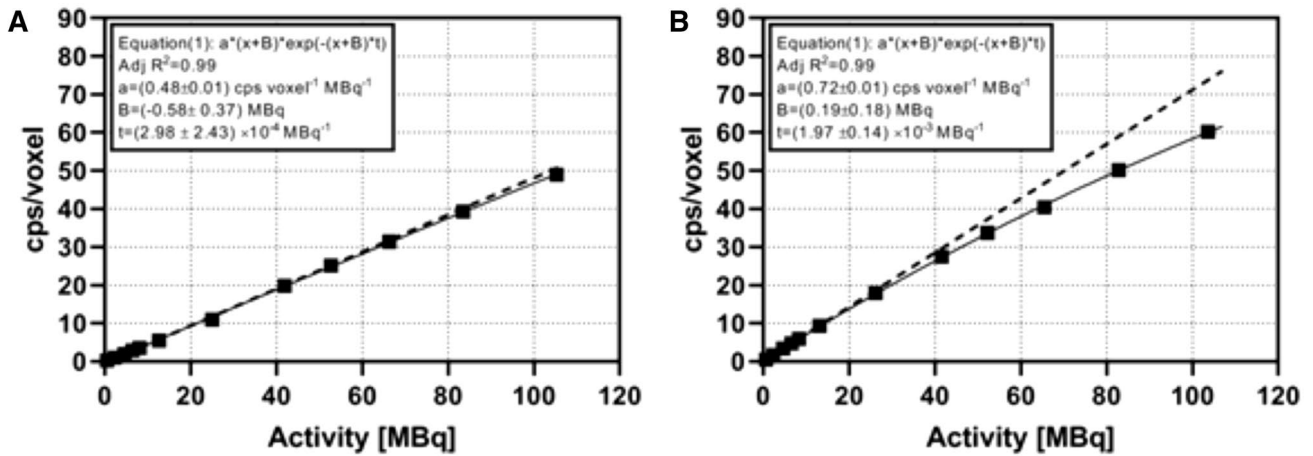


Fig. 4 Radioactivity and SPECT image counts linearity for the SPH (a) and MPH (b) configuration with the fit parameters obtained from the paralyzable system function Eq. (1). The straight line corresponds to the case with $t=0$ MBq⁻¹. MPH configuration shows slight bend-

ing for higher activities because of five times higher counts as compared to the SPH configuration, however, (Eq. 1) was successfully used to describe this bending and can be used for correcting the deviation

based on the visualization of the fitted graphs (Figs. 3b and 4b), coefficient of variation of the fitted parameters (< 50%, except for background activity parameter B for MPH for the system and SPECT image linearity) and adjusted $R^2 \sim 1$. The typical activity used in pre-clinical imaging is around 4–30 MBq [11, 13]. The purpose of using the high activity of 100 MBq in our study was to determine the paralyzable function parameter t in order to investigate the effect of the dead-time. However, the activity of 100 MBq would be too high to be used in a pre-clinical imaging study.

with the point source was 23.10 ± 0.3 cps/MBq (SPH) and 105.6 ± 5.5 cps/MBq (MPH).

The overall sensitivity measured with the NEMA phantom was 15.7 ± 0.1 cps/MBq (SPH) and 69.2 ± 0.1 cps/MBq (MPH). The sensitivity measured at the center of the FOV

Region of interest (ROI) analysis

According to the minimum Var, the OSEM reconstruction algorithm converged with 12 iterations for all the rods (Fig. 5) and with 2 to 4 iterations for the uniform region. The corresponding RC values for the 5 mm, 4 mm, 3 mm and 2 mm rods were 0.60 ± 0.28 , 0.61 ± 0.24 , 0.29 ± 0.11 and 0.20 ± 0.06 (SPH) and 0.56 ± 0.20 , 0.50 ± 0.18 , 0.38 ± 0.09 and 0.23 ± 0.06 (MPH), respectively (Fig. 6). The RC of 1 mm rod of the NEMA phantom was not distinguishable from the background in the image for both SPH and MPH.

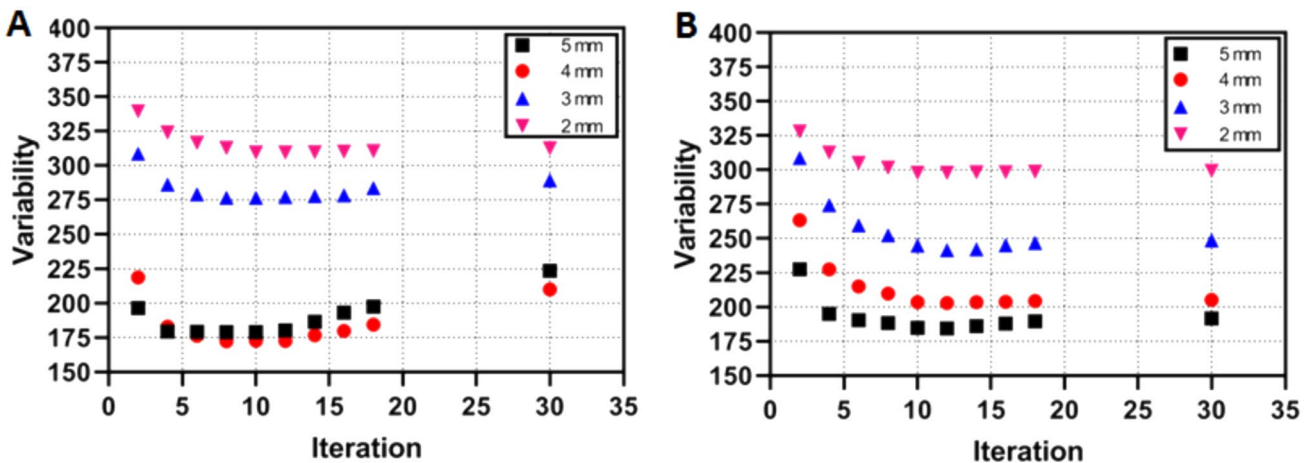


Fig. 5 Convergence of the OSEM reconstruction algorithm based on the calculation of the variability for the individual rods with the SPH (a) and MPH (b) configuration, with increasing number of iterations

Therefore, the RC of 1 mm was not analyzed and was not reported.

Spatial resolution

The spatial resolution of the system for the SPH and MPH configurations was calculated at the center of the detector’s FOV (80 mm FOV setting) for the x, y and z directions based on the method described in “Spatial resolution” section. The values of FWHM for the axial, tangential and radial

orientation corrected for the source’s dimensions, were 2.51 mm, 2.54 mm, and 2.55 mm for the SPH and 2.35 mm, 2.44 mm and 2.32 mm for the MPH, respectively (Table 1).

Image uniformity

The calculated image uniformity in both the MPH and the SPH configurations increased with higher activities (Fig. 7a) and decreased with higher numbers of iterations (Fig. 7b). The relative deviation of the integral uniformity between

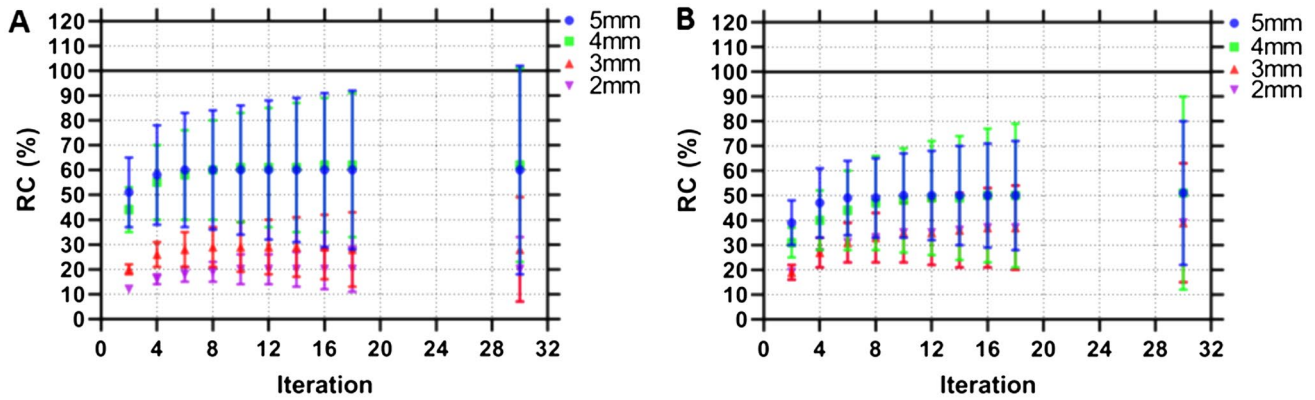


Fig. 6 Recovery coefficient values for the 5 mm, 4 mm, 3 mm and 2 mm rods of the NEMA image quality phantom with (a) SPH and (b) MPH collimation systems for different iteration numbers

Table 1 Spatial resolution (FWHM and FWTM) was calculated based on the methods described in “Spatial resolution” section, for the SPH and MPH collimation system

	Axial		Tangential		Radial	
	SPH	MPH	SPH	MPH	SPH	MPH
FWHM (mm)	2.51	2.35	2.54	2.44	2.55	2.32
FWTM (mm)	4.78	4.32	4.77	4.45	4.95	4.78

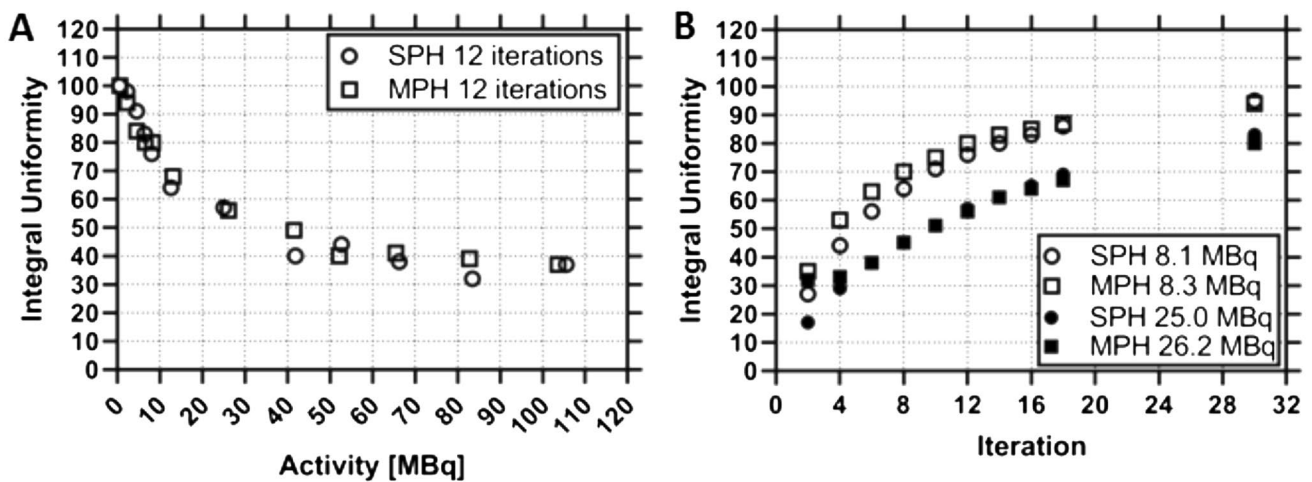


Fig. 7 Integral uniformity as a function of activity with 12 iterations (the OSEM reconstruction algorithm converged with this iteration number, Fig. 5) (a) and number of iterations (b) for both the SPH and the MPH configurations

MPH and SPH configuration was $(2.2 \pm 9.1)\%$ (Fig. 7a). Based on the results in Fig. 7b, the relative deviation of the integral uniformity between MPH and SPH configuration for activity of 25.03 MBq and 8.10 MBq were $(-4.9 \pm 15.4)\%$ and $(-7.6 \pm 7.5)\%$, respectively.

Discussion

The performance of the S102 SPECT sub-system of the ALBIRA II tri-modal imaging system was investigated for the 80 mm FOV with the single pinhole (SPH) and multi-pinhole (MPH) collimators using ^{99m}Tc and the influence of the imaging characteristics on the accuracy of activity quantification was determined.

The sensitivity of a SPECT system depends on factors such as the pinhole aperture diameter, the number of pinholes and the distance between the imaged object and the pinholes [17, 18]. The sensitivity measured with the NEMA point source was higher than that measured with the NEMA IQ phantom (32% (SPH) and 34% (MPH) higher) due to geometry (different source sizes and shapes) and attenuation effects of the NEMA IQ phantom. However, this result was expected, as the value calculated using the NEMA IQ phantom is more realistic for the analysis in the preclinical setting.

In Figs. 3 and 4, the response (cps) of the system and SPECT image counts increases linearly with activity for the SPH configuration. A slight bending is observed for higher activities indicating detector saturation for the MPH configuration. The paralyzable system function (Eq. 1) was successfully used to fit the data and to describe this bending (Figs. 3 and 4) and can be used for correcting the deviation. The detector in the MPH configuration receives about five times more counts than for the SPH configuration [1]. This is reflected in a reduced sensitivity at higher activity and is visible as slight bending of the curve in Fig. 3b (effect of the detector dead-time).

Based on the calculation of the Var (Eq. (2)) [14], the OSEM algorithm converged with 12 iterations for all rods and for both pinhole configurations (SPH and MPH, Fig. 5). Figure 6 shows the effect of the limited system resolution (spill-over effect) and the partial volume effect to the RC values. The maximum recovery of the activity concentration in the 5 mm rod was around 60%. This result signifies the effect of partial volume when the lesion size is less than three times the FWHM of the image resolution [19, 20].

The spatial resolution calculated at the center of the 80 mm FOV shows that the MPH configuration may have a marginally (around 6%) better resolution than SPH (Table 1). However, since a measurement of the uncertainty is not possible for the calculation of the FWHM with the method described in “Spatial resolution” section, it is difficult to

estimate the FWHM difference between the SPH and the MPH configurations. Overall, the spatial resolution of the system with both SPH and MPH configuration was ~ 2.5 mm for the FOV of 80 mm. Note that previous studies with the ALBIRA I system with smaller FOVs have already shown higher resolution capabilities of the system (FWHM < 1 mm for a FOV setting of 20 mm) [11, 13]. The spatial resolutions calculated for the ALBIRA II system in this study are lower (around 21% for SPH and 7% for MPH) than the spatial resolutions of the ALBIRA I system reported by Sanchez et al. [11] for the 80 mm FOV. The spatial resolutions of the ALBIRA I and the ALBIRA II for the SPH/MPH specifications are 2.00 mm/2.20 mm and 2.53 mm/2.37 mm, respectively. The origin of the differences is unclear as there are many confounding factors like the phantoms used for the analysis, the methods used for the calculation of the FWHM, the reconstruction algorithms and the noise levels of the measurements. Specifically, the uncertainties are not given for the FWHM values by Sanchez et al. [11] and in our study (the FWHM calculation using the NEMA method does not provide the uncertainty). Thus, these differences could possibly be attributed also to the uncertainties.

Due to the physical constraints, the SPH collimator has low detection efficiency, and the aim of the MPH collimator is to improve the sensitivity while maintaining the spatial resolution. The spatial resolution of the MPH configuration was approximately the same as that of the SPH configuration while the sensitivity of the MPH configuration is around five times higher (Table 2 and [11]). Although Fig. 6a and b also show that the recovery coefficient values for the 5 mm and 4 mm rods are higher for the SPH as compared to the MPH, these are within the range of the respective standard deviations. Therefore, based on results from this study the MPH configuration is recommended for future in-vivo studies.

Several studies have shown analyses of different preclinical SPECT systems previously [21–26]. Table 2 shows a comparison of different generations of pre-clinical SPECT systems available including the 80 mm FOV of the ALBIRA II SPECT system investigated in this study. From this table, we can see the influence of the number of detector pairs, collimator design and the size of the FOV on the resolution and the sensitivity of a SPECT system. The comparison refers to settings for rat acquisitions. The ALBIRA system offers the possibility to use different collimators and FOV sizes. Hence, the SPECT resolution of ALBIRA system ranges from 0.8 mm with FOV 20 mm [11] to 2.53 mm with FOV 80 mm (this study) and the sensitivity value ranges from 700 cps/MBq for a FOV of 20 mm [11] to 105 cps/MBq for a FOV of 80 mm (this study). Based on 80 mm FOV, ALBIRA II SPECT system investigated in this study has a comparable spatial resolution and sensitivity with the tierSPECT system (Table 2). ALBIRA II SPECT system has even five times higher sensitivity than tierSPECT for the MPH configuration. Based on this evidence,

Table 2 Comparison of different pre-clinical SPECT systems to evaluate the potential in-vivo imaging in rats

System	Detector type	Collimator	FOV (mm)	Resolution FWHM (mm)	Sensitivity (cps/MBq)
NanoSPECT R UHR [23]	4 Rotating detector heads	MPH (9), Ø 1.5 mm	60	1.10	599
TierSPECT [12]	1 Rotating detector head	Parallel hole, Thickness 1 mm	82	2.08 (object-detector distance 30 mm)	22
XSPECT [24]	4 Rotating detector heads	MPH (5), Ø 0.50, 0.75, 1 mm	125	0.5–2.0	620
YAP-(S)PET [25]	2 Rotating detector heads	Parallel hole, thickness 0.6 mm	40	3.5	114
ALBIRA I SPECT [11] ^a	2 Rotating detector heads	SPH, MPH (5), Ø 1 mm	80	2.00 (SPH), 2.20 (MPH) ^c	19 (SPH), 80 (MPH) ^c
ALBIRA II SPECT ^{a,b}	2 Rotating detector heads	SPH, MPH (5), Ø 1 mm	80	2.53 (SPH), 2.37 (MPH) ^c	23 (SPH), 105 (MPH) ^c

^aBoth studies use the SPECT S102 system

^bThis study

^cNote that the sensitivity and spatial resolution differences between ALBIRA I SPECT in the literature [11] and the ALBIRA II SPECT in this study might come from the methodology (e.g. source type employed). However, as the uncertainty is not given in the numbers, it is unclear if there is a difference

the ALBIRA II SPECT system has a favorable performance and can be used as a valuable tool for pre-clinical studies.

The percentage of integral uniformity (calculated using Eq. 4) is higher for a lower activity and hence the higher the activity the more uniform the image (Fig. 7a). For an activity of around 40 MBq the image reached a plateau (Fig. 7a). SPH and MPH show a similar integral uniformity for the image reconstruction with 12 iterations (Fig. 7a), although due to the higher sensitivity (and consequently lower statistical noise) a better uniformity could be expected for the MPH configuration. This may be attributed to the image reconstruction algorithms. For high iteration numbers the MPH configuration yields images with (slightly) better uniformity (Fig. 7b). The better SPH integral uniformity for lower iteration numbers indicates a possible optimization of the image reconstruction algorithm for the MPH configuration, specifically with respect to the start of the algorithm.

In general, the ALBIRA II SPECT system has shown favorable physical characteristics. The measured physical characteristics of the system are comparable to other commercial systems, e.g. the ALBIRA I SPECT and TierSPECT system, for the 80 mm FOV based on sensitivity and spatial resolution. Therefore, pre-clinical studies for the development of new diagnostic and therapeutic radiopharmaceuticals can be performed using the ALBIRA II SPECT system with the recovery coefficients and spatial resolution shown in this study.

Conclusion

In this study, the performance of the S102 SPECT camera system was assessed for the 80 mm FOV. The Sodium doped Cesium Iodide (CsI(Na)) continuous single crystal detectors

resulted in a pre-clinically valuable sensitivity even for the investigated large FOV configuration. The spatial resolution was comparable to the current pre-clinical systems in the market. The ability of quantitative image reconstructions was evaluated based on the recovery coefficients that showed suitable values. Overall, the system performed adequately for the investigated radionuclide and the results indicate that the system is a valuable tool for small animal imaging.

Acknowledgements The authors would like to thank the colleagues from Bruker Biospin GmbH, Ettlingen, Germany for the helpful discussions during the course of this research. This research project is part of the Research Campus M²OLIE and funded by the German Federal Ministry of Education and Research (BMBF) within the Framework “Forschungscampus – public-private partnership for Innovations” under the funding code 13GW0388A and 13GW0091E.

References

1. Franc BL, Acton PD, Mari C, Hasegawa BH. Small-animal SPECT and SPECT/CT: important tools for preclinical investigation. *J Nucl Med.* 2008;49:1651–63.
2. Khalil MM, Tremoleda JL, Bayomy TB, Gsell W. Molecular SPECT imaging: an overview. *Int J Mol Imaging.* 2011. <https://doi.org/10.1155/2011/796025>.
3. Seo Y, Jiang H, Franc BL. *Preclinical SPECT and SPECT/CT, in molecular imaging in oncology.* Heidelberg: Springer; 2013.
4. Beyer T, Freudenberg LS, Townsend DW, Czernin J. The future of hybrid imaging-part 1: hybrid imaging technologies and SPECT/CT. *Insights Imaging.* 2011;2:161–9.
5. Golestani R, Wu C, Tio RA, Zeebregts CJ, Petrov AD, Beekman FJ, et al. Small-animal SPECT and SPECT/CT: application in cardiovascular research. *Eur J Nucl Med Mol Imaging.* 2010;37:1766–77.
6. Vallabhajosula S. *Molecular imaging. Radiopharmaceuticals for PET and SPECT.* Berlin: Springer; 2009.
7. Glatting G, Bardiès M, Lassmann M. Treatment planning in molecular radiotherapy. *Z Med Phys.* 2013;23:262–9.

8. Hardiansyah D, Attarwala AA, Kletting P, Mottaghy FM, Glatting G. Prediction of time-integrated activity coefficients in PRRT using simulated dynamic PET and a pharmacokinetic model. *Phys Med.* 2017;42:298–304.
9. Jiménez-Franco LD, Kletting P, Beer AJ, Glatting G. Treatment planning algorithm for peptide receptor radionuclide therapy considering multiple tumor lesions and organs at risk. *Med Phys.* 2018;45:3516–23.
10. Attarwala AA, Karanja YW, Hardiansyah D, Romanó C, Roscher M, Wängler B, et al. Investigation of the imaging characteristics of the ALBIRA II small animal PET system for ^{18}F , ^{68}Ga and ^{64}Cu . *Z Med Phys.* 2017;27:132–44.
11. Sánchez F, Orero A, Soriano A, Correcher C, Conde P, Gonzalez A, et al. ALBIRA: a small animal PET/SPECT/CT imaging system. *Med Phys.* 2013;40:051906.
12. Wirrwar AK, Nikolaus S, Schramm NU, Arkian S, Cohnen M, Müller HW [TierSPECT: performance of a dedicated small-animal-SPECT camera and first in vivo measurements]. *Z Med Phys.* 2005;15:14–22.
13. Spinks TJ, Karia D, Leach MO, Flux G. Quantitative PET and SPECT performance characteristics of the Albira Trimodal pre-clinical tomograph. *Phys Med Biol.* 2014;59:715–31.
14. Glatting G, Reske SN. Treatment of radioactive decay in pharmacokinetic modeling: influence on parameter estimation in cardiac ^{13}N -PET. *Med Phys.* 1999;26:616–21.
15. Attarwala AA, Hardiansyah D, Romanó C, Roscher M, Molina-Duran F, Wängler B, et al. A method for point spread function estimation for accurate quantitative imaging. *IEEE Trans Nucl Sci.* 2018;65:961–9.
16. NEMA. Performance measurements of small animal positron emission tomographs. Rosslyn: NEMA Standard Publications; 2008. (NU 4).
17. Beekman FJ, van der Have F, Vastenhouw B, van der Linden AJ, van Rijk PP, Burbach JP, et al. U-SPECT-I: a novel system for submillimeter-resolution tomography with radiolabeled molecules in mice. *J Nucl Med.* 2005;46:1194–200.
18. Metzler SD, Bowsher JE, Smith MF, Jaszczak RJ. Analytic determination of pinhole collimator sensitivity with penetration. *IEEE Trans Med Imaging.* 2001;20:730–41.
19. Soret M, Bacharach SL, Buvat I. Partial-volume effect in PET tumor imaging. *J Nucl Med.* 2007;48:932–45.
20. Togawa T, Yui N, Kinoshita F, Yanagisawa M. Quantitative evaluation in tumor SPECT and the effect of tumor size: fundamental study with phantom. *Ann Nucl Med.* 1997;11:51–4.
21. Takahashi Y, Miyagawa M, Nishiyama Y, Ishimura H, Mochizuki T. Performance of a semiconductor SPECT system: comparison with a conventional Anger-type SPECT instrument. *Ann Nucl Med.* 2013;27:11–6.
22. Umeda IO, Tani K, Tsuda K, Kobayashi M, Ogata M, Kimura S, et al. High resolution SPECT imaging for visualization of intratumoral heterogeneity using a SPECT/CT scanner dedicated for small animal imaging. *Ann Nucl Med.* 2012;26:67–76.
23. Schramm N, Hoppin J, Lackas C, Gershman B, Norenberg J, de Jong M. Improving resolution, sensitivity and applications for the NanoSPECT/CT: a high-performance SPECT/CT imager for small-animal research. *J Nucl Med.* 2007;48:436P.
24. Deleye S, van Holen R, Verhaeghe J, Vanderberghe S, Stroobants S, Staelens S. Performance evaluation of small-animal multipinhole μSPECT scanners for mouse imaging. *Eur J Nucl Med Mol Imaging.* 2013;40:744–58.
25. Nikolaus S, Wirrwar A, Antke C, Kley K, Müller HW [State-of-the-art of small animal imaging with high-resolution SPECT]. *Nuklearmedizin.* 2005;44:257–66.
26. van der Have F, Vanstenhouw B, Ramakers RM, Branderhorst W, Krahl JO, Ji C, et al. U-SPECT-II: an ultra-high-resolution device for molecular small-animal imaging. *J Nucl Med.* 2009;50:599–605.

Publisher's Note Springer Nature remains neutral with regard to jurisdictional claims in published maps and institutional affiliations.